An Experimental Study on Energy Absorption Capability of Cast and 3D Printed Architected Cement-based Materials

Koichi Imagawa*, *Motohiro* Ohno and *Tetsuya* Ishida

Department of Civil Engineering, Graduate School of Engineering, The University of Tokyo, Tokyo, 113-8656, Japan

Abstract. Previous studies have demonstrated that Architected Cement-based Materials (ACMs), which have architected internal configurations at mm-cm scale, can have desired and/or unusual mechanical characteristics that the brittle base material does not possess. 3D Concrete Printing (3DCP) is promising technology to fabricate the complicated geometry of ACMs, but relevant research and development are still scarce. In this study, we fabricated truss-type ACMs with enhanced specific energy absorption capacity by either casting or 3D-printing. The ACM was designed by a generative design framework that integrates reinforcement learning and nonlinear structural analysis. The performances of the ACMs were evaluated by uniaxial compression tests. The cast series showed same trend in the cracking characteristics as the simulation. However, the printed ACM showed significantly lower strength and energy absorption than the simulation result. Unexpected damage localization was observed in the printed ACM, especially around the corners of the truss members where relatively large voids tend to be formed during 3D-printing. The degree and location of these defects can be partly controlled by the printing path, which was not considered in the simulation. Therefore, to realize high-performance ACMs by 3DCP, base material properties, internal geometry, and printing path should be simultaneously considered in the design process.

1 Introduction

In recent years, several studies have shown that Architected Cement-based Materials (ACMs), which have architected internal configurations at mm to cm scale, can exhibit intended and/or unusual mechanical characteristics that the brittle base material does not possess [1–9]. Moini et al. investigated the application of biomimetic Bouligand architectures in cementitious materials, and demonstrated enhanced toughness and controlled crack propagation in the inherently brittle material [9]. Sajadi et al. also reported that the adoption of Schwarzite structure could significantly enhance the toughness of cement-based materials [6]. Xu et al. fabricated an auxetic structure with fiber-reinforced cementitious materials [5,7]. The composite exhibited a negative Poisson's ratio under uniaxial compression.

---

* Corresponding author: imagawa@concrete.t.u-tokyo.ac.jp

Although most existing research on ACMs is limited to relatively small test specimens fabricated by using formworks, those studies clearly suggested the potential of ACMs.

3D Concrete Printing (3DCP), which can produce complex geometries by extruding cementitious materials layer by layer, has been intensively being developed in recent years, and is promising technology to apply ACM designs to large scale structures. However, many studies have reported that mechanical properties of hardened 3D-printed concrete are different from those of traditional cast concrete [10–22]. There are many studies that report anisotropic compressive, tensile, and flexural strengths of 3D-printed specimens; these are considered to be caused by many factors such as mix design of printable material and printing parameters [10,11,17–21]. It is also observed that interlayer strength can be significantly affected by printing parameters and environmental conditions [12–16,22]. Since there are only a few reports that focus on 3D-printed ACMs until today, it is still unclear what kind of performance differences might arise between cast ACMs and 3D-printed ones.

The aim of this study is to experimentally study the differences in performance between a 3D-printed ACM and a cast one from the perspective of volumetric energy absorption capacity, and to clarify the mechanisms that give rise to the differences. We fabricated two ACMs using fiber-reinforced cement mortar: cast specimen and 3D-printed specimen. Their mechanical performances were evaluated through uniaxial compression tests while measuring the surface strains by the Digital Image Correlation (DIC) [23]. The obtained surface strain distributions of the two specimens were compared, and their mechanical behaviors and failure mechanisms were investigated.

2 Experimental Program

2.1 Cast ACM

2.1.1   ACM Design

Figure 1 illustrates the ACM design investigated in this study. This design was generated by a computational generative design framework proposed by Ohno et al. [24]. In the design framework, a large number of ACM designs can be randomly generated within any design space, and their mechanical properties are evaluated by nonlinear structural analysis based on finite element method (FEM). Also, this design framework includes deep reinforcement learning algorithm that evolves ACM designs based on the simulation results, which enables efficient exploration of ACM designs that possess desired mechanical properties.

The ACM design shown in Fig. 1 was generated with the above design method, aiming to maximize a specific energy absorption (SEA) under uniaxial compression. Here, the SEA means absorbed energy divided by a volume of the ACM. The energy absorption is calculated from the area under the load displacement curve for a range of 0 to 20 mm displacement; this range corresponds to 0 to 10 % effective strain that is determined to eliminate collisions between finite elements. The effective strain means the overall displacement of the ACMs relative to the height of the design space (i.e., 200 mm).

COM3 [25], which is a structural analysis software based on FEM and includes constitutive laws of fiber-reinforced mortar (FRM) [26,27], was used to evaluate mechanical properties of ACMs. In this ACM design generation, FRM, whose detail will be explained in Section 2.1.2, was assumed as the base material.

Figure 2 depicts the simulated relationship between effective stress and effective strain (left) and the maximum principal strain map at the peak stress (right). The effective stress is

calculated by dividing the applied load by the section area of the design space (i.e., 200 mm * 40 mm = 8000 mm^2). The maximum effective stress and SEA of the ACM are 1.39 MPa and 36.5 kJ/m^3, respectively. From the strain distribution, this design seems to resist the external force mainly by the vertical columns that carry a large part of the overall compressive load while dissipating damages to the diagonal links at the four corners. Thus, it is suggested that this ACM effectively leverages the compressive capacity of the base FRM even with a limited amount of material usage.
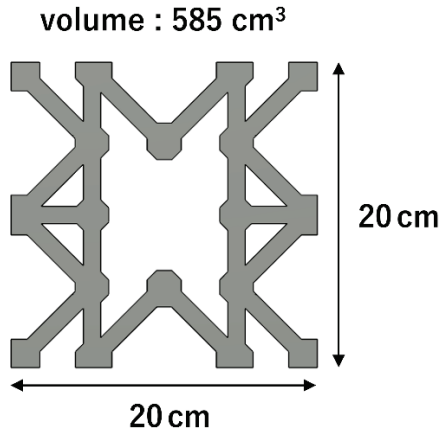

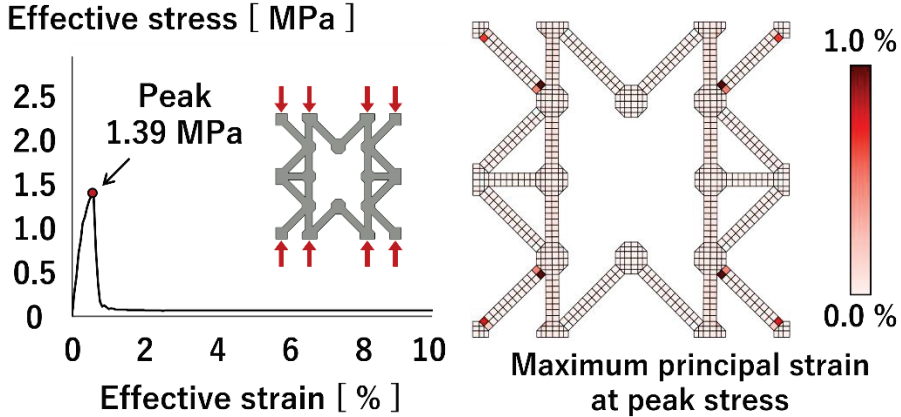**Fig. 1.** Investigated design for cast ACM specimen. Thickness is 4 cm.

Fig. 2. Simulated effective stress-effective strain curve under uniaxial compression and maximun principal strain map of cast ACM design.

2.1.2   Specimen Preparation

Table 1 presents the mix design of the FRM used as the base material of the ACM. The FRM has a water to binder ratio of 26% and includes short basalt fibers ($\Phi 17\mu m \times 10mm$) with volume fraction of 1.5%. Compressive strength of the FRM was obtained by uniaxial compression test on cylindrical specimens ($\Phi 5cm \times 10cm$). The tensile performance was measured by uniaxial tension test on dogbone specimens. Both of the measurements were carried out at 7 days after casting the specimens. The average mechanical properties are shown in Table 2.

Table 1. Mix design of FRM (each value is a mass ratio relative to Ordinary Portland Cement).

Ordinary Portland Cement	Fly ash	Silica sand	Water	Super plasticizer	Basalt fiber ($V_f =$ 1.5%)
1.00	2.80	0.95	0.99	0.027	0.12

Table 2. Compressive and tensile properties of FRM at age of 7 days.

Compressive strength	First cracking strength	Ultimate tensile strength	Tensile strain capacity	Strain failure
18.6 MPa	0.54 MPa	3.3 MPa	0.059 %	0.58 %

One ACM specimen was prepared by casting the FRM in a mold that was produced using a commercially available plastic resin 3D printer. Uniaxial compression test was carried out on the ACM specimen at 7days after the casting while measuring the surface strains by DIC. To mitigate undesirable friction, Teflon sheets were inserted between the specimen and the loading head of the testing machine. The load was measured by the load cell. Crosshead displacement of the compression testing machine was recorded as the overall displacement.

2.2 3D-printed ACM

2.2.1 ACM Design

Figure 3 illustrates the ACM design for a 3D-printed specimen. This design is same as the cast ACM shown in Fig.1, but its size is made larger considering the precision of the 3D mortar printer.

Figure 4 depicts the simulated relationship between effective stress and effective strain (left) and the maximum principal strain map at the peak stress (right). In the simulation, FRM for 3DCP, which will be mentioned below, was assumed as the base material. The maximum effective stress and SEA of the ACM are 8.50 MPa and 281.7 kJ/m3, respectively. Both of the mechanical properties are larger than the cast ACM, which would be attributed to the higher compressive capacity of the base material. From the strain distribution, concentrated strains can be found in the diagonal links at the four corners, and vertical columns still have capacity to further carry the load. In simulation, the same failure mechanisms are found between the cast ACM design and the 3D-printed one regardless of the base materials.
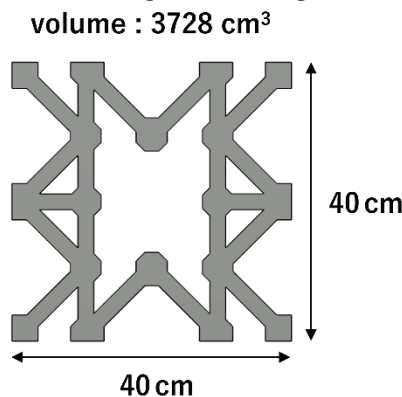

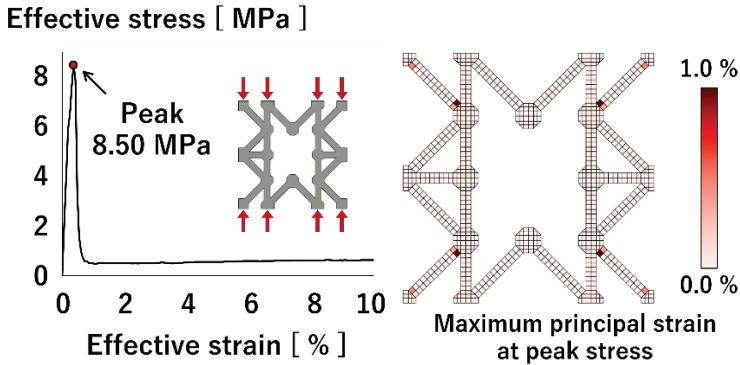**Fig. 3.** Investigated design for 3D-printed ACM specimen. Thickness is 8 cm.

Fig. 4. Simulated effective stress-effective strain curve under uniaxial compression and maximun principal strain map of 3D-printed ACM design.

2.2.2   Specimen Preparation

Printable FRM was prepared for 3D-printing an ACM specimen. Its compressive strength was 143.11 MPa, which was measured by uniaxial compression test on a $\Phi5 \times 10$-cylinder specimen after curing for more than 100 days. The ACM specimen was fabricated with a 3D mortar printer that is based on extrusion technique of cementitious material with a six-axis robotic arm [28]. Table 3 lists printing parameters.

Table 3. Process parameters of 3D printing.

Nozzle shape	Nozzle size (diameter)	Layer height	Filament width
Circular nozzle	10 mm	5 mm	10 mm

Plaster was applied around the loading points of the 3D-printed ACM specimen for making flat surface to prevent stress concentrations. Uniaxial compression test was conducted at the age of more than 100 days. Teflon sheets were placed between the specimen and the loading heads to eliminate undesirable confining stress as much as possible. The load was measured by the load cell. Crosshead displacement of the compression testing machine was recorded as the overall displacement. Surface strains of the specimens were measured by DIC.

3   Result and Discussion

Figure 5 shows the effective stress versus effective strain curve and the distribution of maximum principal strain obtained from a uniaxial compression test of the cast ACM specimen. The specimen showed the maximum effective stress of 2.51 MPa at an effective strain of 0.76 %. After that, the stress sharply decreased, but an increasing trend in the stress was observed thereafter. The measured SEA was 81.7 kJ/m3.

As shown in the strain map, a localized strain occurred on the lower right diagonal link at the peak stress and then, some cracks were formed around the vertical column with the decrease in the effective stress. Similar failure tendency as the simulation was observed.

As mentioned above, the measured stress increased again after the first peak, which resulted in higher SEA than the simulation result. This was caused by the interlocking of the crack surfaces; this phenomenon cannot be considered in the current simulation model and its experimental reproducibility cannot be guaranteed. However, it would be possible to

realize further improvements in the energy absorption capacity by designing an internal structure that intentionally causes such interlocking.
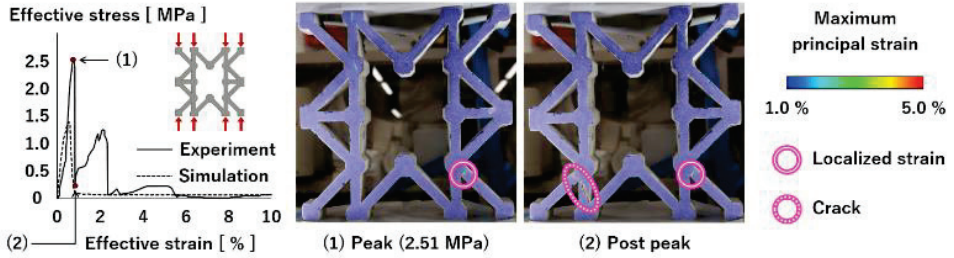

Fig. 5. Measured effective stress versus effective strain curve and maximun principal strains (cast ACM specimen).

Figure 6 displays the effective stress versus effective strain curve and the map of maximum principal strain obtained from a uniaxial compression test on the 3D-printed ACM specimen. The measured maximum effective stress and SEA were 0.22 MPa and 2.47 kJ/m³, respectively. Both of them are significantly lower than the simulation results.

From the strain distribution map, it can be observed that localized strains occurred at two locations at the peak stress. However, these locations are different from those expected by the simulation; in the simulation, strains were expected to concentrate in the diagonal members at the four corners (Fig. 4). This unexpected and localized damage is thought to be attributed to the printing path. Relatively large voids tend to occur especially at the corners of the printing path, which could affect the load transmission path, leading to the reductions in the maximum stress and SEA. Furthermore, insufficient bonding between mortar filaments might also be one of causes for the reduced mechanical performance.

While the effects of those voids and interlayer bonding are not considered in the current simulation, their location and degree can be partly controlled by the printing path. The current ACM design framework focuses on representing the mechanical performance based on properties of the base material and internal geometry, but the printing path is also an important factor for the design of ACMs fabricated by 3DCP.
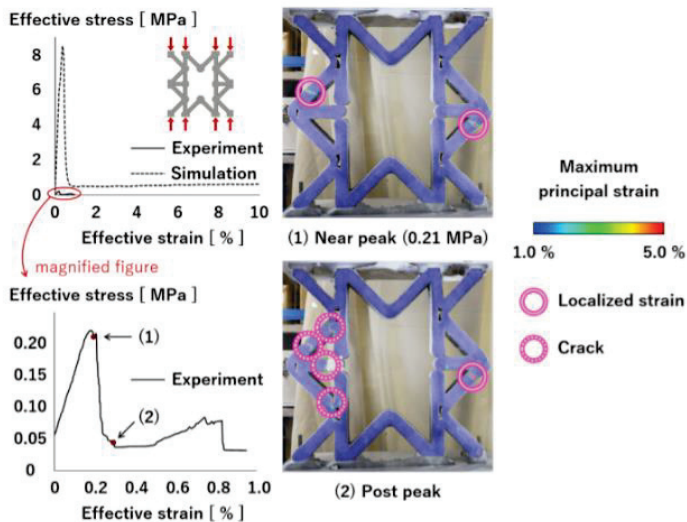

Fig. 6. Measured effective stress versus effective strain curve and maximun principal strains (3D-printed ACM specimen).

4 Conclusion

Compression tests were carried out on a cast ACM and a 3D-printed ACM to investigate the differences in performance between them. The observed failure mechanism of the cast specimen agreed with the simulation. However, in the experiment of the printed ACM, the observed trend in the cracking characteristics was strongly affected by relatively large voids and weak interlayers between mortar filaments, resulting in the significantly lower maximum stress and SEA than the simulated values. The degree and location of those voids and interlayers can be partly controlled by the printing path. Therefore, the printing path should be considered in the design process to realize high-performance ACMs by using 3DCP.

References

1. Y. Xu and B. Šavija, Eng Struct **294**, (2023)
2. K. Barri, Q. Zhang, J. Kline, W. Lu, J. Luo, Z. Sun, B. E. Taylor, S. G. Sachs, L. Khazanovich, Z. L. Wang, and A. H. Alavi, Advanced Materials **35**, (2023)
3. K. Nishijo, M. Ohno, and T. Ishida, in (2022), pp. 139–144
4. Z. Gan, Y. Zhuge, D. P. Thambiratnam, T. H. T. Chan, T. Zahra, and M. Asad, International Journal of Protective Structures **13**, 295 (2022)
5. Y. Xu, E. Schlangen, M. Luković, and B. Šavija, Constr Build Mater **266**, (2021)
6. S. M. Sajadi, C. S. Tiwary, A. H. Rahmati, S. L. Eichmann, C. J. Thaemlitz, D. Salpekar, A. B. Puthirath, P. J. Boul, M. M. Rahman, A. Meiyazhagan, and P. M. Ajayan, IScience **24**, (2021)
7. Y. Xu, H. Zhang, E. Schlangen, M. Luković, and B. Šavija, Cem Concr Compos **111**, (2020)
8. J. A. Rosewitz, H. A. Choshali, and N. Rahbar, Cem Concr Compos **96**, 252 (2019)
9. M. Moini, J. Olek, J. P. Youngblood, B. Magee, and P. D. Zavattieri, Advanced Materials **30**, (2018)
10. M. van den Heever, A. du Plessis, J. Kruger, and G. van Zijl, Cem Concr Res **153**, (2022)
11. M. K. Mohan, A. V. Rahul, G. De Schutter, and K. Van Tittelboom, Cem Concr Compos **115**, (2021)
12. Y. Weng, M. Li, D. Zhang, M. J. Tan, and S. Qian, Cem Concr Res **143**, (2021)
13. A. J. Babafemi, J. T. Kolawole, M. J. Miah, S. C. Paul, and B. Panda, Sustainability (Switzerland) **13**, (2021)
14. Z. Geng, W. She, W. Zuo, K. Lyu, H. Pan, Y. Zhang, and C. Miao, Cem Concr Res **138**, (2020)
15. Y. Chen, K. Jansen, H. Zhang, C. Romero Rodriguez, Y. Gan, O. Çopuroğlu, and E. Schlangen, Constr Build Mater **262**, (2020)
16. G. Ma, N. M. Salman, L. Wang, and F. Wang, Constr Build Mater **244**, (2020)
17. J. Zhang, J. Wang, S. Dong, X. Yu, and B. Han, Compos Part A Appl Sci Manuf **125**, (2019)
18. B. Lu, Y. Weng, M. Li, Y. Qian, K. F. Leong, M. J. Tan, and S. Qian, Constr Build Mater **207**, 477 (2019)
19. A. V. Rahul, M. Santhanam, H. Meena, and Z. Ghani, Constr Build Mater **227**, (2019)
20. V. N. Nerella, S. Hempel, and V. Mechtcherine, Constr Build Mater **205**, 586 (2019)

21. R. A. Buswell, W. R. Leal de Silva, S. Z. Jones, and J. Dirrenberger, Cem Concr Res **112**, 37 (2018)
22. J. G. Sanjayan, B. Nematollahi, M. Xia, and T. Marchment, Constr Build Mater **172**, 468 (2018)
23. H. Schreier, J.-J. Orteu, and M. A. Sutton, *Image Correlation for Shape, Motion and Deformation Measurements* (Springer US, Boston, MA, 2009)
24. M. Ohno, M. Pierre, K. Imagawa, and T. Ishida, Journal of Building Engineering **65**, (2023)
25. K. Maekawa, H. Okamura, and A. Pimanmas, *Non-Linear Mechanics of Reinforced Concrete* (CRC Press, 2003)
26. B. Suryanto, K. Nagai, and K. Maekawa, *Modeling and Analysis of Shear-Critical ECC Members with Anisotropic Stress and Strain Fields* (2010)
27. B. Suryanto, K. Nagai, and K. Maekawa, ACI Mater J **107**, 450 (2010)
28. C. Gosselin, R. Duballet, P. Roux, N. Gaudillière, J. Dirrenberger, and P. Morel, Mater Des **100**, 102 (2016)